geosciences

MDPI

Article

A Theory of Abrupt Climate Changes: Their Genesis and Anatomy

Hsien-Wang Ou

Lamont-Doherty Earth Observatory, Columbia University, Palisades, NY 10964, USA; hsienou0905@gmail.com

Abstract: We combine our ice-sheet and climate models to formulate a deductive theory of abrupt climate changes pertaining to Heinrich/Dansgaard–Oeschger (H/DO) cycles and the last deglaciation punctuated by the Younger Dryas (YD). Since they are all accompanied by ice-rafted debris, we posit their common origin in the calving of the ice sheet due to a thermal switch at its bed, which naturally endows abruptness to these climate signals of the millennial timescale characteristics of the ice-mass balance. To distinguish the H/DO cycles, we differentiate the thermal triggers by geothermal-heat/surface-melt in the calving of inland/coastal ice, which provide their respective freshwater sources. Since surface-melt requires post-H warmth during the glacial, but is already operative in the Holocene, the DO cycles are encased within the H cycle during the glacial, but self-sustaining in the Holocene. They otherwise share the same time signature, thus resolving this seeming puzzle of commonality without invoking unknown climate forcing. The DO cycles transcend deglaciation to produce the observed sequence, but the calving-induced freshwater flux needs to be boosted by the rerouting of continental meltwater to cause YD. We discern a key process of an eddying ocean in its millennial adjustment toward maximum entropy production (MEP), which would melt the H-induced sea ice to cause an abrupt post-H warming followed by a gradual cooling that anchors the DO cycles to form the hierarchical Bond cycle. Since the modelled anatomies resemble the observed ones, our theory may provide a robust and unified account of abrupt climate changes.

Keywords: abrupt climate change; Heinrich events; Dansgaard–Oeschger cycles; bond cycles; younger dryas; ice-sheet instability; maximum entropy production

Citation: Ou, H.-W. A Theory of Abrupt Climate Changes: Their Genesis and Anatomy. *Geosciences* **2022**, *12*, 391. https://doi.org/10.3390/geosciences12110391

Academic Editors: Jesus Martinez-Frias, Xianglei Li and Yijia Liang

Received: 8 August 2022
Accepted: 17 October 2022
Published: 24 October 2022

1. Introduction

The last ice age was teeming with abrupt climate changes pertaining to Heinrich/Dansgaard–Oeschger (H/DO) cycles and deglaciation punctuated by the Younger Dryas (YD), a dramatic climate reversal. While these climate signals are distinct, they are all accompanied by ice-rafted debris (IRD) [1] (their Figure 6), [2] (their Figure 3), [3] (their Figure 7), suggesting their common origin in the calving of the ice sheet. It is well recognized that a large ice sheet is unstable to geothermal heating to periodically calve the inland ice [4]—the source of the IRD layer that defines the H event (HE), —and the accompanying freshwater flux would elicit a climate response, as manifested in the H cycles [5]. Since the DO cycles are associated with quite smaller freshwater flux [6] (their Figure 3), their originating calving must involve only peripheral ice; such calving of inland/coastal ice as the two-tiered IRD sources of the H/DO cycles is indeed supported by observational analysis [7], which will be put on a firmer physical footing in our theory.

Since the thermal switch of ice calving operates on a very short (years) subglacial hydrological timescale [8], it would generate step-like freshwater flux to endow abruptness to the climate signal of the millennial timescale, the latter being characteristic of the ice-mass balance [9]. Forgoing such step-like forcing, numerical calculations have sometimes boosted the freshwater forcing to effectuate hysteresis between ocean modes hence the observed abruptness [10,11], and being anchored on the same ocean modes, the H/DO cycles would have comparable amplitude with interstadials being in effect the interglacial [11]—both at odds with observation. Here we should first note that although the DO cycles are associated

with a large surface-air temperature (SAT) signal [12], the latter simply reflects the extremely cold winter air of stadials due to the extensive sea ice [13,14] whereas the correlative sea-surface temperature (SST) and meridional overturning circulation (MOC) are in fact quite muted [2]—in comparison with the H cycles—and both their interstadials are distinctly non-interglacial [15] (their Figure 2b). Besides forced mode switches, they may also be self-sustaining, as manifested in the so-called "deep decoupling" oscillation [16], which can be millennial when diapycnal diffusivity, a free parameter [17], is properly tuned [18], but being anchored on ocean modes, they are similarly contravened by observation.

In addition to the mode change, the DO cycle has also been modelled as relaxation oscillation of the ocean when it is subjected to freshwater hosing, stochastic atmosphere or an unbalanced initial state [16,19–24]. The period, being related to the ocean overturning time [16], depends critically on the MOC strength [19], a sensitivity that is difficult to reconcile with similar millennial pacing of the glacial and Holocene DO cycles [1] with vastly different MOCs. In the Holocene, incidentally, such relaxation oscillation is what manifests in the Atlantic multidecadal variability [25,26] not the millennial DO cycles. The shared time signature of the glacial and Holocene DO cycles suggests a common genesis [1], so the small Holocene signal of no more than 2 °C further negates the interpretation of the glacial DO cycles as involving mode change.

Tellingly, when step-like freshwater fluxes are applied to a climate model [27], they yield abrupt climate changes proportional to the forcing, which clearly dispels the misconception that abruptness equates mode change [28,29]. In our conception, in contrast, the abruptness simply reflects the step-like freshwater perturbation coupled with the decadal ocean response [30], and its signal span is proportional to the forcing hence can be small, as seen during the Holocene. Since the freshwater flux in [27] is tuned to produce the observed climate signal, it remains a diagnostic study and their interstadials do not exhibit the characteristic cooling [12], both these deficiencies will be remedied in our theory. As required for a deductive theory however, we shall integrate ice-sheet and climate models that have been previously developed by this author [31,32], both of which entail critical but overlooked physics, as previewed next.

In the ice-sheet model, we shall differentiate thermal triggers by geothermal-heat/surface-melt, which would calve inland/coastal ice, the respective freshwater sources of the H/DO cycles. The physical closure has removed an entrenched empiricism regarding the sliding velocity [9], so the prognostic surge properties can be justifiably imposed as an external forcing of the ocean. In addition, since surface-melt predicates on post-HE warmth during the glacial time but is already operative in the Holocene [33], one expects the glacial DO cycles to be embedded in the H cycle while the Holocene DO cycles to be self-sustaining yet retaining the same time signature, thus resolving these seeming puzzles [34]. For the climate model, we shall underscore a key process of an eddying ocean, namely, it would be propelled on the millennial timescale toward maximum entropy production (MEP). This "MEP adjustment" evidently provides a robust account of some salient features of the Bond cycle, including the abrupt post-HE warming followed by a gradual cooling that anchors the DO cycles to exhibit their hierarchical structure.

To isolate the governing physics, we seek a *minimal* model which, with lesser latitude for tuning, allows a more critical test against observation. This minimalistic approach is diametrically opposite to simulation models, which seek *maximal* physics to improve the realism—often at the expense of their falsifiability. These opposite approaches must be kept in mind when assessing our model simplifications. Given the crudeness of the model and the wide range of observed parameter values, we simply select their *plausible* values to produce the generic anatomy for observational comparison.

For the organization of the paper, we shall first discuss the essence of the ice-sheet (Section 2) and climate (Section 3) models, which are applied in Sections 4–6 to address the H/DO cycles and deglaciation sequentially. Within each section, we highlight their salient observed features, discuss their genesis and anatomy based on model physics, and provide a synthesis of previous studies for comparison. We conclude the paper in Section 7.

2. The Ice-Sheet Model

Readers are referred to [32] for a detailed derivation of the ice-sheet model, the following discussion however suffices for self-containment. That a large ice sheet is unstable to geothermal heating to exhibit quasi-periodic surge was first proposed by [4] and subsequently demonstrated in ice-sheet models [9]. Physically, ice growth by accumulation would increasingly trap the geothermal heat to warm the bed to the pressure-melting point when a surge is triggered; the ensuing thinning would augment the conductive cooling to refreeze the bed, terminating the surge. As the thermal switch is also favored by greater driving stress, it is sited off the ice divide to calve inland ice discharged through the Hudson Strait, and the ejected icebergs would strew IRD throughout the subpolar water, as seen in the thinning IRD layer following their drift path [35]. Numerical simulations of the surge cycle, however, often involve tuning of the sliding velocity [9], which directly impacts its amplitude and period. This empiricism is removed in [32] by the global momentum balance [36], so the model closure allows us to prognose surge properties.

A tangible outcome of the model is the construction of a 2-D regime diagram (Figure 1) whereby surging properties are contoured against length/width of the discharging ice, all are nondimensionalized (hence primed) by scales defined by the climate condition (Table 1), so they can be readily assessed for both varying climate and ice-sheet dimensions. The model has delineated three dynamical regimes: steady-creep, steady-sliding and cyclic-surge separated by thick and shaded lines, which can be understood as follows. For a short stream, the frictional creep can absorb the accumulation to maintain a steady state, so the thermal switch remains off. For a longer stream, the thermal switch would turn on to trigger the sliding motion whose speed, however, depends on the strait width: for a narrower strait hence slower sliding, the ice flux can be sustained by a catchment to maintain a steady state, but for a wider strait hence faster sliding, the ice flux cannot be sustained, resulting in surge cycles.

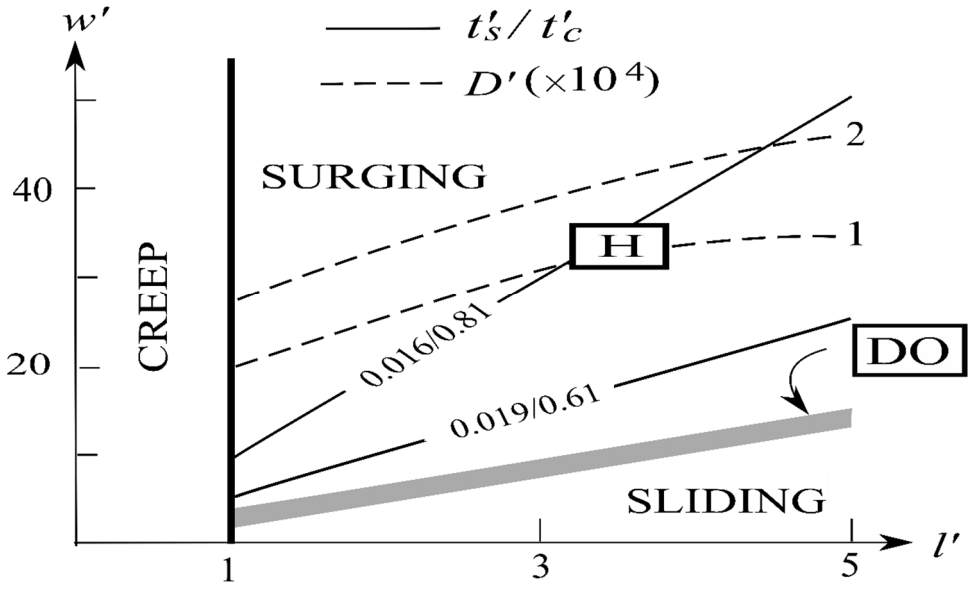

Figure 1. A regime diagram whereby discharge rate (thin dashed line) and surge/creep duration (thin solid line) of the surging ice are plotted against its length/width, all nondimensionalized by scales listed in Table 1. It consists of three dynamic regimes of steady-creep, steady-sliding and cyclic-surge separated by thick and shaded lines. Boxes H and DO mark the H and DO cycles.

Table 1. Differing ice-discharge parameters for H/DO (starred are from limit-cycle solution). Other (common) values are listed in Appendix A.

		Definition	Unit	H	DO
$\dot{a}$	Accumulation		m y^{-1}	0.3	0.1
$\dot{g}$	Geothermal heating		10^{-2} Wm^{-2}	6	3
$[h]$	Height scale		km	3	0.5
$[t]$	Time scale	$[h]/\dot{a}$	ky	10	5
w	Half-width		km	100	12.4 *
$[w]$	Scale of w	$[h]$	km	3	0.5
l	Longitudinal distance		km	500	100
$[l]$	Scale of l	$(\rho_i g)^{1/2}(3\dot{a}\nu)^{-1/2}[h]^2$	km	142	6.8
$[a]$	Aspect ratio scale	$[w][l]^{-1}$		0.021	0.074
τ	Driving stress	$\rho_i g[h]^2 l^{-1}$	bar	1.62	0.23
$[\tau]$	Scale of τ	$\rho_i g[h]^2[l]^{-1}$	bar	5.7	3.3
u	Surge velocity	$u = \tau w^2(3\nu[h])^{-1}$	m y^{-1}	4500	59 *
$[u]$	Scale of u	$[h][\tau](3\nu)^{-1}$	m y^{-1}	14.3	1.4
D	Discharge rate	$2w[h]u$	Sv	0.09	2.3×10^{-5} *
$[D]$	Scale of D	$2[w][h][u]$	10^{-6}·Sv	8.2	2.2×10^{-2}
α_h	Heating parameter	$[\tau][u]\dot{g}^{-1}$		4.3	0.48

Relevant to the present study, we have contoured discharge rate $D^{'}$ and surge/creep duration (t_s'/t_c') in the regime diagram, and the H box marks the ice discharge through the Hudson Strait, which indeed falls well within the cyclic-surge regime in support of its postulated origin of H cycles. Dimensional discharge rate can be directly derived, as seen next. Since driving stress is:

$$\tau = \rho_i g[h]^2/l \tag{1}$$

where ρ_i is the ice density, g, the gravitational acceleration, $[h]$, the height of ice divide and l, the length of Hudson Strait, and the surge velocity subjected to the global momentum balance [36] is:

$$u = \tau w^2/(3\nu[h]) \tag{2}$$

where w is the half-width of Hudson Strait and ν, the ice viscosity, they render a discharge rate of:

$$D = 2w[h]u = 2\rho_i g[h]^2 w^3/(3\nu l) \tag{3}$$

Setting $[h]/w/l$ =3/100/500 km [37] and $\nu = 400$ bar y [32], the discharge rate is 0.09 Sv. Since the total discharge into the subpolar water would be augmented by calving from the surrounding ice sheet synchronized by sea-level coupling [7,9] (it is thus of the same order as that inferred from observation [38], contrary to the shortfall contended by [39]. Setting, additionally, accumulation of $\dot{a} = 0.3$ my^{-1} and geothermal heating of $\dot{g} = 0.06$ Wm^{-2}, surge/creep durations shown in Figure 1 are 0.16/7 ky, which are consistent with the observed 5–10 ky period of the H cycle [40] (their Figure 3). Since observation has not falsified these surge properties deduced from the ice-sheet model, they may be justifiably imposed as the external forcing of the ocean.

Since the DO cycle has a freshwater flux that is significantly smaller than the H cycle [6] (their Figure 3), its calving likely involves only the coastal ice. Searching for clues that might differentiate the two, we note that the englacial ice-sheet temperature shows two distinct zones of temperate bed [41] (their Figure 4d): besides the one under the ice dividing due to the geothermal heat, there is another one in the ablation zone where the surface-melt

is particularly effective in warming the bed via vertical advection. We posit therefore, that the DO cycle is driven by the thermal switch under the equilibrium line, which would calve the coastal ice of the ablation zone. Unlike the ice discharge through the Hudson Strait, this shallow calving can occur along an open ice front, as seen in west Antarctic ice streams [42] and from numerical calculations over a flatbed [43]. The latter additionally provide an apt demonstration of a plausible scenario: following the thermal trigger, the surging ice would grow in width until it is arrested by a limit cycle, resulting in periodic self-organized ice streams.

Since the thermal switch underpinning Figure 1 is generic, the limit cycle is precisely the boundary that divides the steady-sliding and cyclic-surge regimes (shaded line, marked DO). Denoting the corresponding "stream" properties by the subscript "s", then the following surging properties are functions only of the heating parameter α_h defined by the relative strength of the frictional to geothermal heating (Appendix A) to be given by:

$$\alpha_h = \rho_i g \dot{a}[h]/\dot{g} \tag{4}$$

where $[h]$ is the equilibrium-line altitude (ELA). Specifically, we derive that the termination height is:

$$h'_s = (1 + 2\alpha_h)^{1/2}/\alpha_h \tag{5}$$

the aspect ratio is:

$$a'_s = \sqrt{2}/h'_s \tag{6}$$

and ratio of surge/creep durations is:

$$t_{ratio} = 2/\left(1 - a'^2_s\right) \tag{7}$$

These are plotted in Figure 2 whose qualitative dependence can be explained as follows: for stronger frictional heating, the ice would be thinner before the conductive cooling may terminate the surge, which in turn would be wider on account of the mass balance, and such a wider surge implies faster sliding motion to shorten the surge relative to the creep phases. Compared with inland ice, coastal ice is thinner, the accumulation is smaller because of the surface-melt/runoff and the geothermal heating is weaker because of less isostatic depression. Therefore, as a plausible example, we set ELA of $[h] = 0.5$ km, accumulation of $\dot{a} = 0.1$ my^{-1}, and geothermal heating of $\dot{g} = 0.03$ Wm^{-2}, which yield a heating parameter of $\alpha_h = 0.48$ (Table 1), as indicated by the dashed line. The resulting fractional surface depression is 0.17, significantly smaller than that of the Heinrich events (greater than 0.5), and the ratio of surge/creep durations is 1.1, both lasting about a millennium. In comparison with the H cycle, the shorter creep is due to the smaller surface drop by surge, which needs less time to be replenished by accumulation, but the surge duration is maintained by the slower sliding, and hence, thinning rate.

Other surge properties are less certain. Setting a longitudinal distance of $l = 100$ km, the stream would be $2w = 24$ km wide with a discharge rate of $D = 2.3 \times 10^{-5}$ Sv (from Equation (3)). We do not know the number of streams emptying into the subpolar water from the surrounding ice sheet, but since the current Greenland has about 300 fast-flowing marine-terminating outlet glaciers [44], it is not unreasonable to assume that there were 1000 such streams during the glacial time because of the much longer ice front, which would yield a total discharge of 0.02 Sv. This is several times smaller than that driving the H cycle, but not inconsistent with their observed sea-level signals [6].

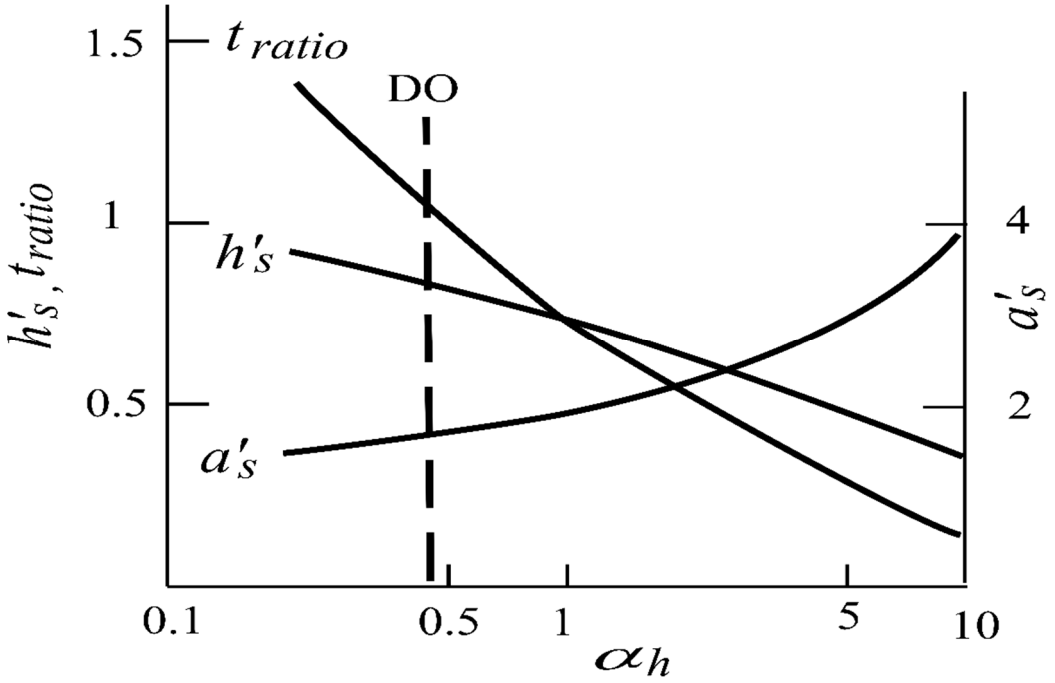

Figure 2. Ice-stream properties of the DO cycle plotted against the heating parameter. They are the termination height h'_s, the aspect ratio a'_s and the ratio of surge/creep durations t_{ratio}. The vertical dashed line is representative of the DO cycle, which shows comparable surge/creep durations.

To recap, we differentiate thermal switches due to geothermal-heat/surface-melt in calving inland/coastal ice that drive the H/DO cycles. Because of the physical closure, the deduced surge properties shown in Figures 1 and 2 are prognostic, so their observational validation justifies their specification as the external forcing of the climate model to be discussed next.

3. The Climate Model

Readers are referred to [31] for the detailed derivation of our climate model, and only the relevant physics are summarized here for self-containment. The model configuration is sketched in Figure 3 in which both ocean and atmosphere are composed of warm/cold boxes aligned at mid-latitudes and continental ice sheet provides anomalous freshwater flux to the subpolar ocean. Since abrupt climate signals are dominated by that of the cold boxes, the model variables are the nondimensionalized cold-box deviations from (known) global-means, and their primes are henceforth dropped to simplify the notation. Other than the freshwater flux, F, the only external forcing is the deficit of the absorbed shortwave (SW) flux (q), which would generate deficits in SST (T), and hence in SAT (not shown) via the convective flux (q_c), the resulting atmospheric heat (hence moisture) transport would induce a salinity deficit (S), which together with the SST deficit specify the density surplus (ρ); the latter drives the MOC (K) across the subtropical front to enter the ocean heat balance.

To illustrate the basic working of our climate model, we draw in Figure 4 the phase-space diagram spanned by the MOC (abscissa) and density surplus (ordinate; markings pertain to temperature), so the climate state is the intersect of two lines: the density curve (thick solid) regulated by thermohaline balance of the ocean and the "MOC line" (sloping dashed) encoding the MOC dependence on density, as discussed next.

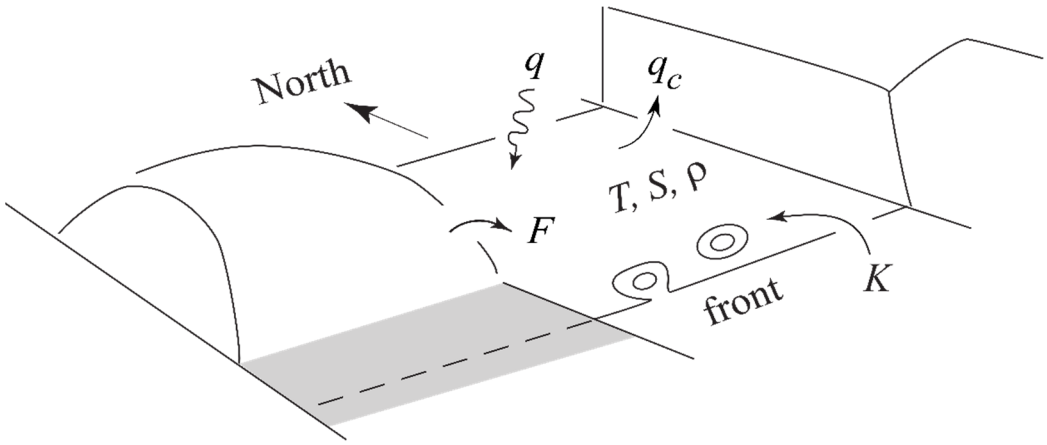

Figure 3. The configuration of the coupled ocean/atmosphere model is composed of warm and cold boxes aligned at mid-latitudes and a continental ice sheet injecting an anomalous freshwater flux into the subpolar ocean. Given the (known) global-mean fields, we examine cold-box deficits in temperature (T), salinity (S), and hence density surplus (ρ), when forced by the cold-box deficit in the absorbed SW flux (q) and the anomalous freshwater flux (F). Internal variables include the MOC (K) and convective flux (q_c) that enter the ocean heat balance.

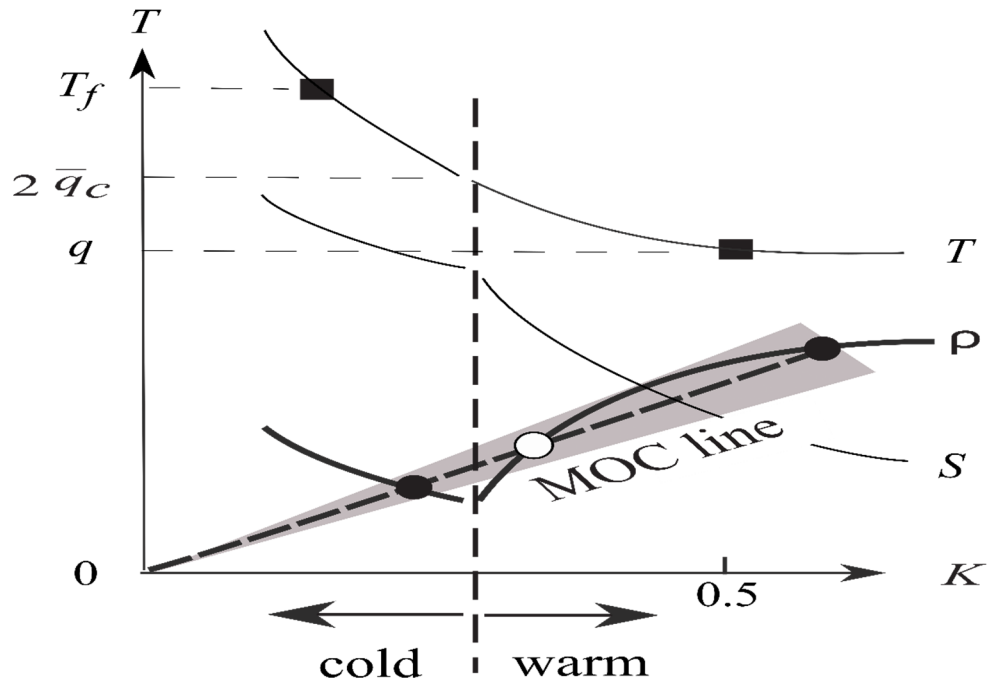

Figure 4. A schematic of the phase-space diagram in which subpolar temperature/salinity deficits (T/S, thin solid lines) and density surplus (ρ, thick solid line) are plotted against MOC (K). The convective bound when the convective flux vanishes (vertical dashed line) divides warm/cold branches. The MOC line (sloping dashed line) pivots on the millennial timescale toward MEP (rectangles), whose intersect with the density curve specifies the climate state (solid ovals, the open oval being the unrealized saddle point). Markings on the ordinate pertain to the temperature.

The density curve represents the spacing between temperature and salinity deficits (thin lines). The decreasing MOC would cool and freshen the subpolar water (hence the rising deficit lines) accompanied by a decreasing convective flux (not shown) hence an increasing atmospheric heat transport. The deficit in the convective flux from its global mean ($\overline{q}_c$) is $T/2$, the factor 2 stemming from concurrent cooling of the surface air, and

since the convective flux may not be negative (that is, the deficit may not exceed the global mean), we discern a "convective bound" at:

$$T = 2\bar{q}_c \tag{8}$$

as indicated by the vertical dashed line. Beyond this convective bound (that is, in lowering MOC), the convective flux would be nil, hence the atmospheric heat transport has saturated at $\bar{q}_c$. As seen from the differing functional dependence of T/S on MOC, the convective bound marks a break in the slope of the density curve, which divides the climate regime into warm/cold branches. In contrast to ocean-only models [45] when the density curve would continue its downward trend to become negative, which has no relevance to the observed ocean, our coupled model allows a normal-signed density contrast through the full range of MOC—because of the convective bound.

As regards the MOC line, it is straight because of the assumed linear dependence of MOC on the density surplus [45,46]. The proportional constant is coined "admittance" drawing its analogy from electrostatics with density/MOC playing the role of voltage/current, whose inverse sets the slope of the MOC line. In primitive-equation models that do not resolve eddies, the MOC takes the form of a laminar overturning cell, and admittance is linked to the diapycnal diffusivity, which in effect is a free parameter finely tuned to yield the observed state [17]. For the example shown in the figure above, the ocean is bistable and the two equilibria (the solid ovals, where the open oval is the unrealized saddle point) are precisely those uncovered by [47] and, in support of our convective bound, their cold state is indeed characterized by a vanishing convective flux [47] (their Figure 18).

In the actual ocean, the admittance is not a free parameter but subjected to microscopic fluctuations associated with random eddy exchange across the subtropical front [48,49]. Applying the fluctuation theorem (FT, a generalized second law) [50], we deduce that the admittance would be self-propelled on millennial timescale toward MEP, a process termed "MEP adjustment". It entails as a special case that the steady-state climate is characterized by MEP [51–53], but the time evolution is needed for addressing abrupt climate change. In addition, FT is of considerable mathematical rigor and has been tested in laboratory [54,55], so its deductive outcome in the steady-state MEP further strengthens the latter's physical basis. For visualization, we have blurred the MOC line to symbolize microscopic fluctuations whose probability bias on account of FT would pivot this line toward MEP, the latter being marked by rectangles and discussed next.

For a box model, the entropy production of the ocean is a product of its heat transport ($K \cdot T$) with the differential temperature T, and one readily sees from Figure 4 that it has a local maximum in the warm branch, which is derived to be $(T,\ K = q,\ 1/2)$ [31] (their Equation (25)). As a cursory check with the current interglacial, the parameter values listed in Appendix A and a subpolar deficit of 100 Wm^{-2} in the absorbed SW flux [56] (their Figure 6.14b with box approximation) would yield a subpolar SST of 6 °C and an MOC transport of 18 Sv (for a 6000-km basin width), both commensurate with the observed ones [57,58]. In the cold branch, the ocean heat transport is fixed by the saturated atmospheric heat transport, so entropy production would increase unabated with cooling until the subpolar water reaches the freezing point ($T = T_f$), which, however, remains free of perennial ice as the latter would reduce the ocean cooling to weaken the MOC, contradicting the MEP. Since MEP adjustment operates on the millennial timescale, the foregoing constraint does not preclude sea-ice formation over a shorter timescale, such as during the HE or winter season. With this recognition, the cold MEP indeed is consistent with the observed LGM characterized by freezing-point subpolar water that remains open in summer [57] (their Figure 15), [59] (their Figure 4). Unlike the tuning of the diapycnal diffusivity in the primitive-equation models mentioned above, MEP contains no free parameters, so its observational test supports the potency of the postulated MEP adjustment.

To recap, climate state is specified by the intersection of the density and the MOC lines in the phase-space (Figure 4). The density line would be displaced by the freshwater flux from ice-sheet dynamics and the MOC line would pivot on the millennial timescale toward

MEP; our task is simply to delineate the time evolution (anatomy) of this intersection, as discussed in the following sections.

4. The H Cycle

4.1. Phenomenology

The last glacial was punctuated by recurring HEs when massive calving of icebergs strewed IRD across the subpolar North Atlantic [5,35,38,60]. The onset and termination of HEs are abrupt and the accompanying freshwater flux is substantial [61] to further depress the MOC from its weak glacial strength [2,62]. Since the subpolar water is already at freezing point [57], a weakening of the MOC would cause formation of extensive sea ice [63], which would deter the melting of icebergs as they drift slowly across the subpolar ocean, as seen in the spatial thinning of the IRD layer [35]. The MOC resumes at the termination of the HE; however, the subpolar water does not just return to the pre-HE glacial state, but an interstadial several degrees warmer [15]. This post-HE warmth is followed by a gradual cooling to exhibit a saw-toothed H-cycle [64,65] albeit the cooling trend is populated by the millennial DO cycles to form the Bond cycle. While SAT registered in Greenland ice cores may vary over O (10 °C), the SST signal is considerably smaller, and the interstadials remain distinctly cooler than the interglacials [15,64]. The substantial variation in the MOC has led to an anti-phased Antarctic climate during the HE outside of which the hemispheric climates remain synchronous [66–68].

4.2. Genesis and Anatomy

The genesis of the H cycle is illustrated in the phase-space diagram shown in Figure 5. The freshwater flux F would displace the density line (thick solid line) and the MOC line (sloping dashed line) would pivot toward the MEP (solid rectangles) in response. The cycle goes through numbered states with solid and dashed arrows indicating abrupt (decadal) changes and the millennial MEP adjustment, respectively. To aid the selection of parameter values, we note that the forcing may vary over 30 Wm^{-2} through the ice age [69] (their Figure 23), but as long as the H cycle remains a glacial phenomenon, it should exhibit a generic anatomy insensitive to forcing. As an illustrative example, we thus set the absorbed SW flux 90 Wm^{-2} below the global mean, the global-mean convective flux at 56 Wm^{-2}, the global-mean SST at 14 °C and the freshwater flux at 0.1 Sv [27,38], so given the scales defined in Appendix A, they yield dimensionless parameters $\left(q, \bar{q}_c, T_f, F\right) = (0.9,\ 0.56,\ 1.75,\ 0.05)$. The corresponding anatomy is drawn in Figure 6 for which we have set surge/creep duration at 1/5 ky with light–dark shades symbolizing freshwater flux and sea-ice cover, respectively.

The H cycle begins with the glacial MEP (State 0) when the thermal switch is turned on and the density line is displaced instantaneously (decadal) by the freshwater flux. Since the MOC line pivoting on the millennial timescale remains immobile, State 0 would transition to State 1 when the weaker MOC would induce extensive sea ice (dark-shaded in the time plot) to maintain the ocean heat balance. During the millennial HE, the MOC line would pivot toward the MEP by melting the sea ice to move State 1 to 2. At the HE termination, the MOC line is again immobile, so State 2 would transition to State 3 to exhibit sudden warming. During the ensuing creep phase, the MEP adjustment would pivot the MOC line toward the glacial MEP (State 0), thus evincing a gradual cooling to form the saw-toothed H cycle.

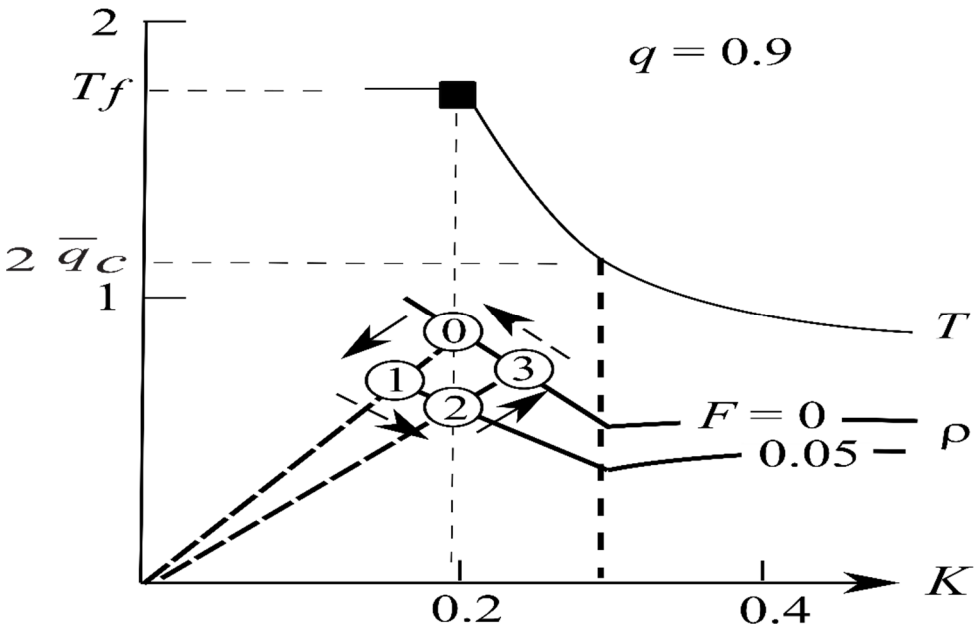

Figure 5. The H cycle in the phase-space when the freshwater flux (F) displaces the density curve (thick solid) and the MOC line (sloping dashed) pivots toward the MEP (solid rectangle) in response. The cycle goes through numbered states with solid and dashed arrows indicating abrupt decadal changes and the millennial MEP adjustments, respectively.

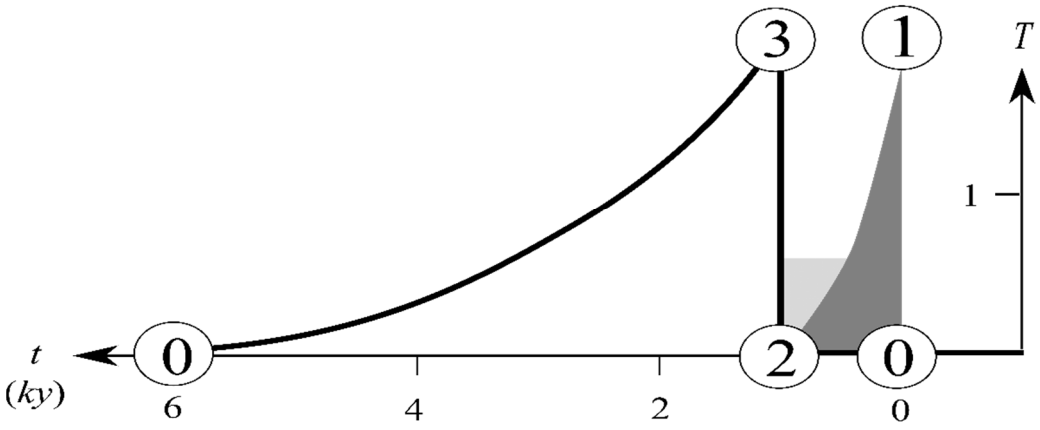

Figure 6. The anatomy in SST (thick solid line) of the H cycle corresponding to that of Figure 5. The light and dark shades symbolize the freshwater flux and sea-ice extent, respectively.

A key property of the H cycle is the post-HE warmth, which can be derived as follows. As the H cycle resides in the cold branch for which the atmospheric heat transport has saturated at the global-mean convective flux $\overline{q}_c$ (Section 3), the total heat transport (given by the orbital forcing q) is partitioned between the atmosphere and the ocean as:

$$q = \overline{q}_c + KT \tag{9}$$

and the salinity balance states:

$$\mu\overline{q}_c + F = KS \tag{10}$$

where μ is the moisture parameter [31] so that the first term is the atmospheric moisture transport, which together with the freshwater flux F are balanced by the salinity flux carried by the MOC. Combining these two equations yields a density surplus:

$$\rho = T - S \tag{11}$$

$$= \frac{1}{K}(q_e - F) \tag{12}$$

where:

$$q_e \equiv q - (1+\mu)\overline{q}_c \tag{13}$$

is a property of the unperturbed state. From Equations (9) and (12) and applying trigonometry, we derive:

$$\frac{T_3}{T_2} = \frac{K_2}{K_3} \tag{14}$$

$$= \frac{\rho_2}{\rho_3} \tag{15}$$

$$= \frac{K_3}{K_2} \cdot \frac{q_e - F}{q_e} \tag{16}$$

so that Equations (14) and (16) yield:

$$\frac{K_2}{K_3} = \left(1 - \frac{F}{q_e}\right)^{1/2} \tag{17}$$

Substituting Equation (17) into Equation (14), we arrive at:

$$\frac{T_3}{T_2} = \left(1 - \frac{F}{q_e}\right)^{1/2} \tag{18}$$

The (dimensional) temperature range (ΔT) of the H cycle is thus:

$$\Delta T = [T](T_2 - T_3) \tag{19}$$

$$\approx \overline{T} \cdot \frac{F}{2\, q_e} \tag{20}$$

for which we have assumed $F/q_e \ll 1$. For parameter values listed in Appendix A, $q_e = 0.17$, so $F/q_e = 0.29$, and Equation (20) yields $\Delta T \approx 2$ °C, as shown in Figure 6. Since this warmth increases with the freshwater flux and summer insolation (decreasing q hence q_e), it would lead to deglaciation when a certain threshold is exceeded, a topic to be discussed in Section 6.

4.3. Synthesis

The post-HE warmth has been attributed to the resumption of MOC, which, however, remains short of the interglacial envisioned for the ocean mode change [10,11]. The subsequent cooling has been ascribed to the downwind effect of a rising ice sheet during the binge phase [64], whose efficacy remains to be demonstrated [70]. In our interpretation, both these features are direct consequences of the MEP adjustment: by melting the sea ice during the HE, it slightly flattens the MOC line, which necessarily yields a warmer state at the HE termination; following this the same process would cool the subpolar water toward the glacial MEP defined by the freezing point. There is thus no need to invoke disparate physics.

With the gradual cooling being the climate response to HE, it does not precondition the next HE [71], which runs on the internal ice clock (Section 2). On the other hand, the primary ice calving through the Hudson Strait could synchronize ice calving from the circum-Atlantic ice sheets via sea-level coupling to augment the freshwater flux [9,35,72]. The sea-ice cover during the HE is induced by the MOC weakened by freshening, which moreover is dissipating through the HE, so a distinct H-mode [29,71] cannot be defined nor is it necessary for explaining abrupt changes. The substantial slowdown of the MOC during the HE would induce an anti-phased Antarctic warming [66–68], outside of which however, the hemispheric climates remain synchronized by global teleconnection [66].

To recap, the interplay between the step-like freshwater flux and the millennial MEP adjustment has produced an H cycle consisting of an abrupt post-HE warming followed by a gradual cooling (Figure 6), an anatomy that is consistent with observation, but not yet adequately simulated by the numerical models.

5. The DO Cycle

5.1. Phenomenology

The cooling phase of the H cycle is populated by the DO cycles [40,73] whose hierarchical structure is intriguing: the DO cycles emerge only after the post-HE warming, and their stadials/interstadials (S/IS) track the cooling trend of the H cycle to form the bundled Bond cycle. The stadials are accompanied by IRD [1,74], just like the HEs, but the freshwater flux is significantly smaller [6], suggesting the calving of the coastal ice [7]. Although the SAT signal is large [12], it is attributable to the extremely cold winter air during the stadials [13] whereas the correlative SST and MOC signals are indistinct [2], which is the reason that the bipolar climate seesaw cannot be discerned for the DO cycles [75]. Unlike the H cycles, the S/IS of the DO cycles have a similar millennial duration, but their transitions remain abrupt and both are slowly cooling to preserve the saw-toothed appearance [76].

Perhaps the most significant observation of the DO cycles is their prevalence in the Holocene even in the absence of a large ice sheet [1,3], which nonetheless share the same millennial pacing as their glacial counterpart, suggesting a common genesis [1,77]. The absence of sea-ice cover renders a much-reduced SAT variation, and together with the further-muted SST and MOC signals they represent merely small perturbations of the interglacial climate.

5.2. Genesis and Anatomy

We have posited in Section 2 that the DO cycles have their origin in the quasi-periodic calving of the coastal ice from the ablation zone. Since there is ablation in the glacial time only by the post-HE warming, the glacial DO cycles are encased within the H cycle, as illustrated in Figure 7, where the outer line represents the H cycle shown in Figure 5. Following the same convention, the DO cycles go through numbered states with solid and dashed arrows indicating the fast (decadal) ocean response and the slow (millennial) MEP adjustment, respectively. The corresponding anatomy is drawn in Figure 8 for which we have applied a square-wave freshwater flux of a 2 ky period (shaded columns) [34] (their Figure 8), and the dark shading symbolizes the sea-ice cover.

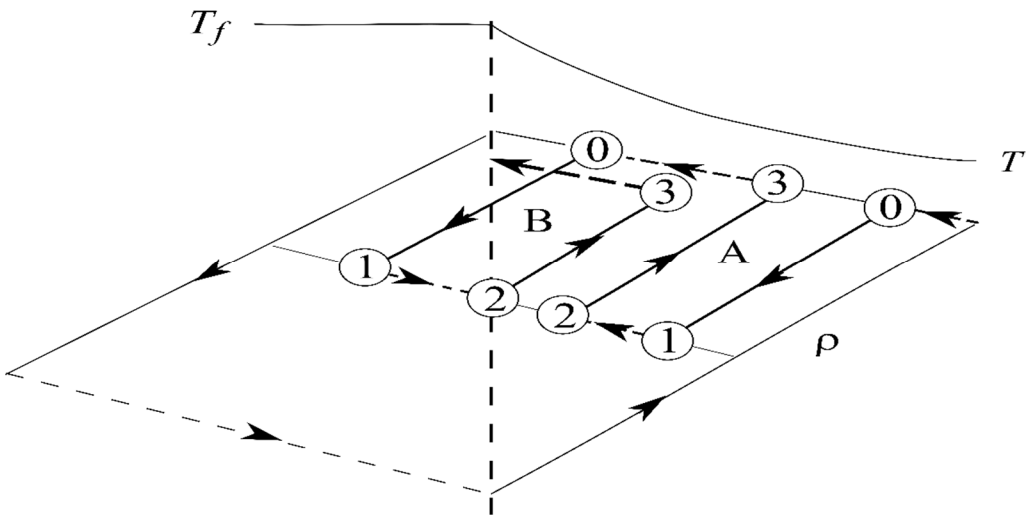

Figure 7. Same as Figure 5, but for DO cycles (thick lines) encased within the H cycle (thin outer lines). Type-A's stadials remain above the freezing point while type-B's stadials have reached the freezing point to resemble a mini-H cycle.

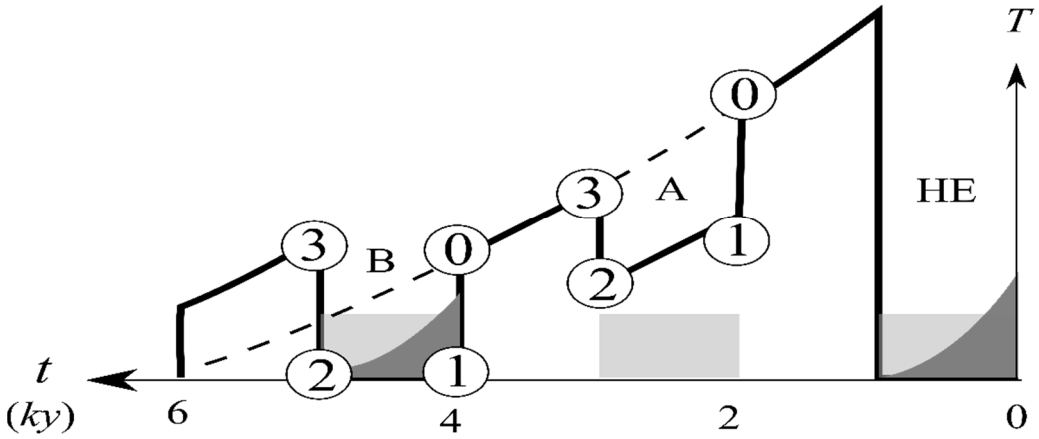

Figure 8. The anatomy (in SST) of the DO cycles corresponding to that shown in Figure 7 when the freshwater flux is a square-wave of a 2 ky period (light shading). Type B's stadial has reached freezing-point to cause formation of the sea-ice (dark shading), resulting in a greater rebound of the ensuing interstadial, but otherwise both the S/IS trend as the H-cooling curve (dashed) to exhibit the hierarchical Bond cycle.

Unlike the H cycle, we distinguish two types of DO cycles, designated as type-A and B. For type-A, the stadial (State 1 to 2) remains above the freezing point and hence is unobstructed in the trending of the H-cooling; therefore, the ensuing interstadial simply returns to the H-cooling curve in the time plot. For type-B however, the stadial has reached the freezing point to cause formation of the sea ice, just like the H cycle, so the ensuing interstadial (State 3) protrudes above the H-cooling curve to resemble a miniature H cycle. This type-B DO cycle is arguably discernible in observation [4] (their Figure 2). Despite the protrusion, both the S/IS trend as the H-cooling to exhibit the hierarchical Bond cycle, as depicted in [64] (their Figure 1).

5.3. Synthesis

Given that the DO cycles are accompanied by IRD [1], but with smaller freshwater flux compared with HEs, we posit their origin in the calving of the coastal ice from the ablation zone, a proposition consistent with the observational analysis [7]. Since during the glacial time, ablation requires post-HE warming, the glacial DO cycles are predicated on the HE hence a large ice sheet; in the Holocene however, ablation is already operative [78] to cause the self-sustained DO cycles. Otherwise, the ice dynamics of the ablation zone should imprint the same time signature on the two, as indeed observed, so there is no need for conjecturing an unknown climate forcing of this commonality [1]. Since the DO cycles are related to the calving of the coastal ice, they are even more susceptible to sea-level coupling to be synchronized among the circum-Atlantic ice sheets [9], which thus may resolve this seeming puzzle as well [79].

Questions have been raised about the causal role of calving because of the IRD lag to the ocean cooling [80]. Such a lag is entailed in the observed embedding of IRD within the stadials [62] (their Figure 7), which however has a simple explanation: upon the calving onset, the ocean would cool within decades [30], which would deter the melting of the icebergs, hence the dislodging of IRD, then even after the calving has ceased, the ocean cannot warm until the icebergs have fully melted. In addition, icebergs from eastern Greenland and the Arctic Ocean could be jammed in the Denmark Strait and their slow drift with the ocean current may cause a downstream delay of IRD [35,74,80]. The apparant IRD lag thus does not negate the calving origin of the DO cycle. Although the ice-shelf instability has also been suggested as a possible driver of the DO cycle [81,82], it does not comport with the attendant IRD signal.

To recap, we propose that the calving of the coastal ice from the ablation zone is the origin of the DO cycle, which endows its abruptness and millennial spacing—common to

both the glacial and the Holocene DO cycles. Since ablation can be set up in the glacial time only by post-HE warming, the glacial DO cycles are encased within the H cycle with their S/IS being gradually cooled by the MEP adjustment to exhibit the hierarchical Bond cycle, as seen in the model-deduced anatomy (Figure 8).

6. Deglaciation

6.1. Phenomenology

The most dramatic abrupt changes occurred during the last deglaciation, which was preceded by the H1 and derailed by a temporary return to a deep freeze in the YD [71]. Multiple freshwater fluxes have been identified, which are accompanied by IRD and retain the millennial pacing of the DO cycles [1] (their Figure 6), [83] (their Figure 6), suggesting their common origin. In addition, there are two massive meltwater pulses (MWP-1A and 1B) derived from the meltback of the Laurentide ice sheet (LIS) by the interglacial warmth [84].

The meltwater is rerouted from the Mississippi to the St. Lawrence rivers when the LIS has sufficiently retreated, which has augmented the calving-induced freshwater flux to cause the YD [85–87]. The coldness of the YD, however, would halt the MWP-1A as seen in the glacial readvance [85], resulting in only a small overlap between the two [88]. Since the LIS has largely disintegrated during the Preboreal, the MWP-1B causes only moderate cooling marking the 8.2 ka event [89]. Despite prominence of the YD, such climate reversal did not occur during penultimate deglaciation [90].

As freshening and cooling have opposite effects on the marine δ^{18}O, they may muddle the interpretation of this data [83]; both H1 and YD, however, manifest strongly in the ice-core δ^{18}O because of the extremely cold winter air [13]. The shutdown of the MOC during these events has caused Antarctic warming and a rising global pCO_2 [66,91], which thus precede the northern climate rebound.

6.2. Genesis and Anatomy

Since the last deglaciation is preceded by the H1, we choose a forcing deficit smaller than that of Figure 5 so the post-HE warmth would vault the climate into the warm branch, as illustrated in Figure 9. For this example, we have set the forcing $q = 0.8$ (that is, the absorbed SW flux is 80 Wm^{-2} below the global mean), and although the freshwater flux is greater for the YD than that that drives the H1, to avoid an unwieldy plot, a single value of 0.1 Sv [86,92] is used in this figure. For the time plot shown in Figure 10, we again assume a square-wave freshwater flux of a 2 ky period (light shading), the same as that that drives the DO cycles, which however can be augmented by meltwater pulses drawn according to their observed timing. Since deduced events resemble observed ones, they are labelled as such to aid the following discussion.

The climate signal begins with the glacial MEP (State 0) and runs through numbered states. The transition from States 0 to 1 to 2 are like the H cycle, but because of the rising summer insolation, the MOC line, flattened by the HE, no longer intersects the density curve in the cold branch at the HE termination, so the climate vaults into the warm branch (State 3), marking the initial deglaciation. Equating the post-HE temperature Equation (18) with the convective bound Equation (8), we derive a criterion for the deglaciation:

$$\frac{F}{q_e} \geq 1 - \left(\frac{2\bar{q}_c}{T_f}\right)^2 \tag{21}$$

The right-hand side (rhs) depends on the global-mean temperature and the convective flux, which set the long-term super-orbital condition; the left-hand side (lhs) on the other hand, depends on the freshwater perturbation and orbital forcing: a greater freshwater flux would cause deglaciation even with a lower summer insolation. Using parameter values listed in Appendix A, the rhs is 0.59, so for a meltwater flux of 0.1 Sv, the deglaciation would occur when the annual absorbed SW flux reaches about 81 Wm^{-2} below the global

mean, as seen in Figure 9. In comparison, the orbital forcing needs to be 8 Wm^{-2} higher without the HE; but since such an insolation increase is attained in about a millennium, the HE may not delay the deglaciation [93] and may possibly even hasten it. On the other hand, since the recurring time of the HE is shorter than half the precession cycle (10 ky), it always punctuates the deglaciation, as is the observed case [94] (their Figure 4).

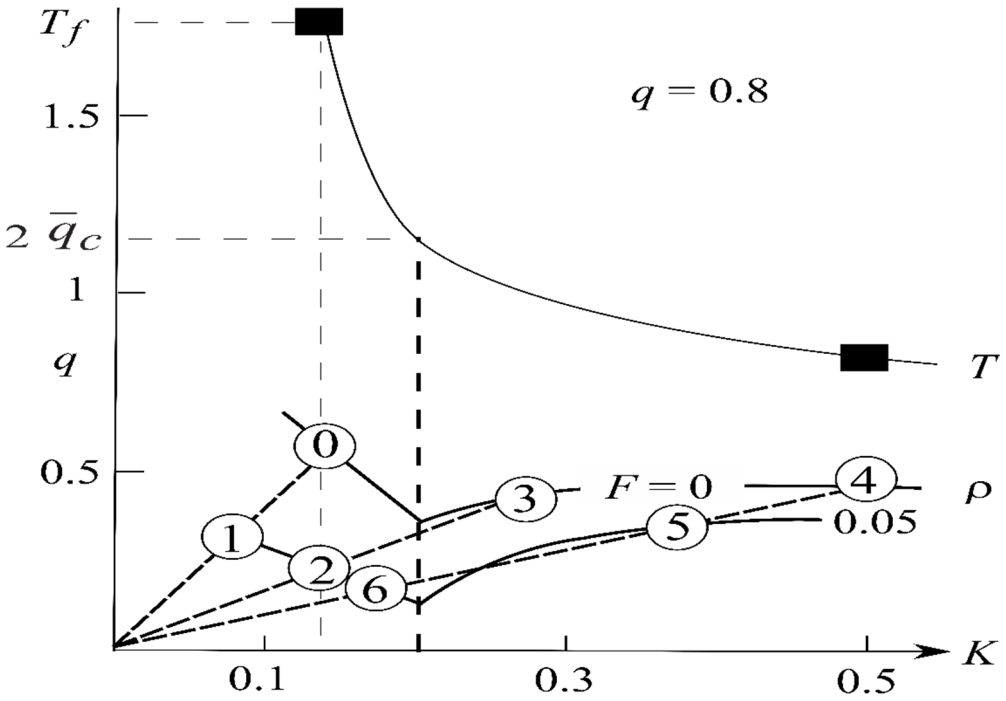

Figure 9. Same as Figure 5 but for $q = 0.8$ to illustrate genesis of the deglaciation (arrows are neglected for clarity).

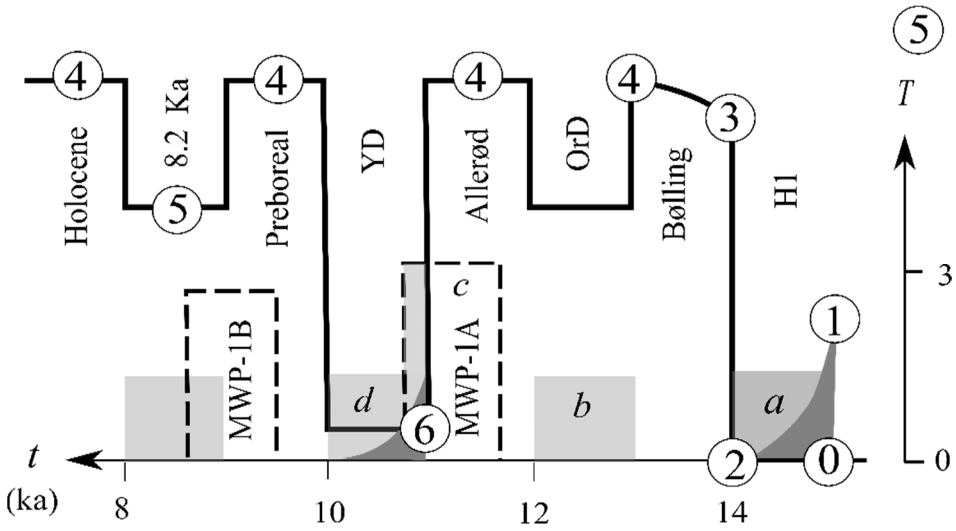

Figure 10. The anatomy of deglaciation corresponding to that of Figure 9 with the observed events labelled. The light shades are the square-wave freshwater flux of a 2-ky period with letters *a*–*d* corresponding to the meltwater events identified in [83]. The dark shades indicate the sea-ice covers induced by ocean cooling.

Following the initial deglaciation, State 3 would propel to State 4 (the warm MEP), a transition spanning the Bølling. The warmth would elevate the snowline to cause calving of the coastal ice after a millennium, just like the DO cycle, and the resulting freshwater flux

would cool State 4 to State 5 marking the Older Dryas (OrD), which, however, remains an interglacial. The continuing Allerød warmth (State 4) would meltback the LIS to generate a massive MWP-1A, but differing from the northern calving, the meltwater does not perturb the climate until the ice margin has sufficiently retreated to allow its rerouting to Hudson Bay. It would then reinforce the calving-induced freshwater flux to further lower the density curve (not drawn) to vault State 4 to State 6 marking the YD. Unlike calving paced by the internal ice dynamics however, the meltback would be halted by the cold YD. Here for simplicity, we have neglected the lesser pivot of the MOC line during the YD because the small density surplus has in effect rigidified the MOC line [31], so termination of the millennial YD would rebound the climate from State 6 to State 4, the latter corresponding to the Preboreal. The recurring ice calving after a millennium causes the 8.2 ka cooling event (State 5), and since the LIS has largely disintegrated during the Preboreal, the MWP-1B is insufficient to cause the glacial flip. After the 8.2 ka event, the climate returns to State 4 corresponding to the Holocene.

6.3. Synthesis

The ultimate driver of deglaciation is the rising summer insolation during increasing eccentricity, the suborbital deglaciation events, however, can be explained by the interplay of three distinct sources of the freshwater perturbation. The first is the calving of the inland ice that triggers the H1, whose post-event warming would vault the glacial into the interglacial. The latter sets up an ablation zone to enable the second source: a quasi-periodic calving of the coastal ice, just like that that drives the millennial DO cycle, whose stadials can be identified with the OrD, the YD and the 8.2 ka event. Contrary to its designation as an HE therefore [71], the YD should be interpreted as a DO-stadial. Given the small freshwater flux associated with calving of the coastal ice, the YD requires a third freshwater source to cause the glacial flip, namely the rerouting of the continental meltwater (MWP-1A). Since the rerouting occurs only after the LIS has sufficiently retreated, and the cold YD would halt the meltback [85], there can only be a small timing overlap between the YD and the MWP-1A [88,95]. This timing mismatch has raised a question about their causal linkage [84], which is now resolved by combining the second and third freshwater sources. Since the YD involves the happenstance of rerouting, it is not inevitable and indeed it did not happen during the MWP-1B or the penultimate deglaciation.

As the YD is accompanied by strong cooling and freshening, they can cancel each other to leave little imprint on the marine δ^{18}O data [71], but it manifests strongly in the ice-core δ^{18}O because of the extensive winter sea ice and cold winter air [13]. The first three freshwater fluxes and the MWP-1A shown in Figure 10 can be identified with the four meltwater events discerned by [83] (their Figure 6), and our model offers a plausible interpretation of their puzzling marine δ^{18}O signature: events *a* and *d* are associated with strong cooling (as symbolized by the shaded sea-ice cover) to cause maxima in the data, but events *b* and *c* involve little cooling, hence they are dominated by freshening to yield minima.

While the YD is triggered by a freshwater flux, its freshening is due primarily to the MOC shutdown [95], which would sequester the southern heat to cause Antarctic warming [66,96,97]. As such, the latter and the accompanying rising pCO_2 would precede the northern climate rebound [91,98], which, however, are not causal since the northern deglaciation is already underway and is only temporarily reversed by the YD due to the internal ice dynamics. The termination of the YD is accompanied by a doubling of accumulation, which has been attributed to atmospheric circulation change [99], but it may simply reflect moister interglacial air, just like that induced by global warming.

That the enhanced moisture transport by global warming may shut down the MOC, like triggering the YD, is a topic widely discussed in the literature [17,31,47]. Model intercomparisons however, show considerable uncertainty in the bifurcation threshold, which may nonetheless be assessed from our model. As the northern summer insolation has dimmed since about 10 ka [71], it would raise the freshwater threshold based on our

phase-space diagram (comparing Figures 5 and 9). However, even the lower threshold and the massive MWP-1B at 8 ka have caused only moderate cooling; there is therefore little prospect of a glacial flip and the next glaciation is likely to be gradual, evolving over a millennial timescale, just like the previous ones. In our conception, only deglaciation and its reversal represent mode changes between the warm/cold branches, which further underscore their generic difference from the in-branch H/DO cycles representing climate perturbations proportional to the freshwater forcing.

To recap, we show that the square-wave freshwater flux of a 2 ky period, the same as that driving the DO cycle, may reproduce the observed deglaciation sequence (Figure 10), including the YD when such flux is augmented by rerouting of the continental meltwater.

7. Conclusions

We combine our ice-sheet and climate models to formulate a deductive theory of abrupt climate changes pertaining to the H/DO cycles and the last deglaciation punctuated by the YD. Since they are all accompanied by IRD, we posit their common origin in the quasi-periodic calving of the ice sheet caused by a thermal switch at its bed. To distinguish the H/DO cycles, however, we differentiate thermal triggers by geothermal-heat/surface-melt in calving inland/coastal ice, hence their respective freshwater source. Since surface-melt requires post-HE warmth during the glacial time, but already operates in the Holocene, the glacial DO cycles are encased within the H cycle, but the Holocene DO cycles are self-sustaining. Otherwise, they share the same time signature of the abruptness of the thermal switch and the millennial timescale characteristic of the ice mass balance; our theory thus may resolve this puzzling commonality without invoking unknown climate forcing.

Besides the common calving source of the freshwater flux, we discern a key process in the ocean response stemming from random eddies, which would propel the MOC toward an MEP on the millennial timescale. This MEP adjustment would melt the HE-induced sea ice to cause a sudden post-event warming followed by a gradual cooling that anchors the DO cycles to form the hierarchical Bond cycle. The same freshwater flux that drives the DO cycles also transcends the deglaciation to produce the observed sequence, which however needs to be augmented by the rerouting of the continental meltwater to cause the YD.

In conclusion, by incorporating the calving-induced freshwater flux and the MEP adjustment of the ocean, our theory has provided a unified account of abrupt climate changes. The modelled anatomies, as exemplified in Figures 6, 8 and 10, resemble the observed ones, in support of our postulated geneses. We contend that, because of the missing physics of MEP adjustment, prior numerical calculations have not adequately simulated the observed abrupt climate changes despite their outward sophistication.

Funding: This research received no external funding.

Institutional Review Board Statement: Not applicable.

Informed Consent Statement: Not applicable.

Data Availability Statement: Not applicable.

Acknowledgments: I want to thank anonymous reviewers whose comments have significantly improved the paper.

Conflicts of Interest: This author declares no conflict.

Appendix A. Symbols

a	Aspect ratio of surging ice
$[a]$	Scale of a $(= [w][l]^{-1})$
$\dot{a}$	Accumulation
$C_{p,o}$	Specific heat of ocean $(= 4.2 \times 10^3$ J Kg^{-1} ^{0}C$^{-1})$
D	Freshwater discharge from ice sheet
$[D]$	Scale of D $(= 2[w][h][u])$
F	Freshwater flux to the ocean $(= 0.1$ Sv$)$
$[F]$	Scale of F $(= 2[K][S]/S_0 = 0.34$ m^{2}s$^{-1})$
g	Gravitation acceleration $(= 9.8$ m s$^{-2})$
$\dot{g}$	Geothermal flux
h	Ice height
$[h]$	Scale of h
K	MOC mass flux
$[K]$	Scale of K $(= \alpha^* L(2\rho_o C_{p,o})^{-1} = 6$ m^{2}s$^{-1})$
l	Longitudinal ice distance
$[l]$	Scale of l $(= (\rho_i g)^{1/2}(3\dot{a}\nu)^{-1/2}[h]^2)$
L	Longitudinal span of cold box
q	Cold-box deficit of absorbed SW flux
$[q]$	Scale of q $(= 100$ Wm$^{-2})$
$\overline{q}_c$	Global convective flux $(= 56$ Wm$^{-2})$
S	Cold-box salinity deficit
S_0	Reference salinity (=35)
$[S]$	Scale of S $(= \alpha[T]/\beta = 1)$
t_c	Creep duration
t_s	Surge duration
t_{ratio}	Ratio of surge/creep duration
$[t]$	Timescale of ice-sheet model $(= [h]/\dot{a})$
T	Cold-box SST deficit
T_f	Freezing-point temperature
$[T]$	Scale of $T(= [q]/\ \alpha^* = 8$ °C$)$
$\overline{T}$	Global-mean SST (=14 °C)
ΔT	Temperature range of H cycle
u	Surging velocity
$[u]$	Scale of u $(= [h][\tau](3v)^{-1})$
w	Half-width of surging ice
$[w]$	Scale of w $(= [h])$
α	Thermal expansion coefficient $(= 10^{-4}$ °C$^{-1})$
α_h	Heating parameter $(= [\tau][u]\dot{g}^{-1} = \rho_i g\dot{a}[h]\dot{g}^{-1})$
α^*	Air–sea transfer coefficient $(= 12.5$ Wm^{-2} °C^{-1}, Ou 2018$)$
β	Saline contraction coefficient $(= 8 \times 10^{-4})$
ρ	Cold-box density surplus
$[\rho]$	Scale of ρ $(= \rho_o \alpha[T] = 0.8$ Kg m$^{-3})$
ρ_i	Ice density $(= 0.92 \times 10^3$ Kg m$^{-3})$
ρ_o	Reference ocean density $(= 10^3$ Kg m$^{-3})$
τ	Driving stress
$[\tau]$	Scale of τ $(= \rho_i g[h]^2[l]^{-1})$
μ	Moisture parameter (= 0.3, Ou 2018)
ν	Ice viscosity $(= 400$ bar y, Ou 2018$)$

References

1. Bond, G.; Showers, W.; Cheseby, M.; Lotti, R.; Almasi, P.; DeMenocal, P.; Priore, P.; Cullen, H.; Hajdas, I.; Bonani, G. A pervasive millennial-scale cycle in North Atlantic Holocene and glacial climates. *Science* **1997**, *278*, 1257–1266. [CrossRef]
2. Elliot, M.; Labeyrie, L.; Duplessy, J.C. Changes in North Atlantic deep-water formation associated with the Dansgaard–Oeschger temperature oscillations (60–10 ka). *Quat. Sci. Rev.* **2002**, *21*, 1153–1165. [CrossRef]
3. Schulz, M.; Paul, A. Holocene climate variability on centennial-to-millennial time scales: 1. Climate records from the North-Atlantic realm. In *Climate Development and History of the North Atlantic Realm*; Springer: Berlin/Heidelberg, Germany, 2002; pp. 41–54. [CrossRef]

4. MacAyeal, D.R. Binge/purge oscillations of the Laurentide ice sheet as a cause of the North Atlantic's Heinrich events. *Paleoceanography* **1993**, *8*, 775–784. [CrossRef]
5. Bond, G.; Heinrich, H.; Broecker, W.; Labeyrie, L.; McManus, J.; Andrews, J.; Huon, S.; Jantschik, R.; Clasen, S.; Simet, C.; et al. Evidence for massive discharges of icebergs into the North Atlantic ocean during the last glacial period. *Nature* **1992**, *360*, 245–249. [CrossRef]
6. Yokoyama, Y.; Esat, T.M. Global climate and sea level: Enduring variability and rapid fluctuations over the past 150,000 years. *Oceanography* **2011**, *24*, 54–69. [CrossRef]
7. Elliot, M.; Labeyrie, L.; Bond, G.; Cortijo, E.; Turon, J.L.; Tisnerat, N.; Duplessy, J.C. Millennial-scale iceberg discharges in the Irminger Basin during the last glacial period: Relationship with the Heinrich events and environmental settings. *Paleoceanography* **1998**, *13*, 433–446. [CrossRef]
8. Fricker, H.A.; Scambos, T.; Bindschadler, R.; Padman, L. An active subglacial water system in West Antarctica mapped from space. *Science* **2007**, *315*, 1544–1548. [CrossRef]
9. Calov, R.; Ganopolski, A.; Petoukhov, V.; Claussen, M.; Greve, R. Large-scale instabilities of the Laurentide ice sheet simulated in a fully coupled climate-system model. *Geophys. Res. Lett.* **2002**, *29*, 2216. [CrossRef]
10. Paillard, D. The hierarchical structure of glacial climatic oscillations: Interactions between ice-sheet dynamics and climate. *Clim. Dyn.* **1995**, *11*, 162–177. [CrossRef]
11. Ganopolski, A.; Rahmstorf, S. Rapid changes of glacial climate simulated in a coupled climate model. *Nature* **2001**, *409*, 153–158. [CrossRef]
12. Johnsen, S.J.; Dahl-Jensen, D.; Dansgaard, W.; Gundestrup, N. Greenland palaeotemperatures derived from GRIP bore hole temperature and ice core isotope profiles. *Tellus B Chem. Phys. Meteorol.* **1995**, *47*, 624–629. [CrossRef]
13. Denton, G.H.; Alley, R.B.; Comer, G.C.; Broecker, W.S. The role of seasonality in abrupt climate change. *Quat. Sci. Rev.* **2005**, *24*, 1159–1182. [CrossRef]
14. Li, C.; Battisti, D.S.; Bitz, C.M. Can North Atlantic sea ice anomalies account for Dansgaard–Oeschger climate signals? *J. Clim.* **2010**, *23*, 5457–5475. [CrossRef]
15. Bard, E. Climate shock-Abrupt changes over millennial time scales. *Phys. Today* **2002**, *55*, 32–38. [CrossRef]
16. Winton, M.; Sarachik, E.S. Thermohaline oscillations induced by strong steady salinity forcing of ocean general circulation models. *J. Phys. Oceanogr.* **1993**, *23*, 1389–1410. [CrossRef]
17. Rahmstorf, S.; Crucifix, M.; Ganopolski, A.; Goosse, M.; Kamenkovich, I.; Knutti, R.; Lohmann, G.; Marsh, R.; Mysak, L.A.; Wang, Z.; et al. Thermohaline circulation hysteresis: A model intercom-parison. *Geophys. Res. Lett.* **2005**, *32*, L23605. [CrossRef]
18. Paul, A.; Schulz, M. Holocene climate variability on centennial-to-millennial time scales: 2 Internal and forced oscillations as possible causes. In *Climate Development and History of the North Atlantic Realm*; Springer: Berlin/Heidelberg, Germany, 2002; pp. 55–73. [CrossRef]
19. Sakai, K.; Peltier, W.R. A dynamical system model of the Dansgaard–Oeschger oscillations and the origin of the Bond cycle. *J. Clim.* **1999**, *12*, 2238–2255. [CrossRef]
20. Timmermann, A.; Gildor, H.; Schulz, M.; Tziperman, E. Coherent resonant millennial-scale climate oscillations triggered by massive meltwater pulses. *J. Clim.* **2003**, *16*, 2569–2585. [CrossRef]
21. Arzel, O.; England, M.H.; De Verdière, A.C.; Huck, T. Abrupt millennial variability and interdecadal-interstadial oscillations in a global coupled model: Sensitivity to the background climate state. *Clim. Dyn.* **2012**, *39*, 259–275. [CrossRef]
22. Peltier, W.R.; Vettoretti, G. Dansgaard-Oeschger oscillations predicted in a comprehensive model of glacial climate: A "kicked" salt oscillator in the Atlantic. *Geophys. Res. Lett.* **2014**, *41*, 7306–7313. [CrossRef]
23. Kleppin, H.; Jochum, M.; Otto-Bliesner, B.; Shields, C.A.; Yeager, S. Stochastic atmospheric forcing as a cause of Greenland climate transitions. *J. Clim.* **2015**, *8*, 7741–7763. [CrossRef]
24. Brown, N.; Galbraith, E.D. Hosed vs. unhosed: Interruptions of the Atlantic Meridional Overturning Circulation in a global coupled model, with and without freshwater forcing. *Clim. Past* **2016**, *12*, 1663–1679. [CrossRef]
25. Kerr, R.A. A North Atlantic climate pacemaker for the centuries. *Science* **2000**, *288*, 1984–1985. [CrossRef]
26. Ou, H.W. A minimal model of the Atlantic multidecadal variability: Its genesis and predictability. *Clim. Dyn.* **2012**, *38*, 775–794. [CrossRef]
27. Menviel, L.; Timmermann, A.; Friedrich, T.; England, M.H. Hindcasting the continuum of Dansgaard-Oeschger variability: Mechanisms, patterns and timing. *Clim. Past* **2014**, *10*, 63–77. [CrossRef]
28. Alley, R.B.; Marotzke, J.; Nordhaus, W.D.; Overpeck, J.T.; Peteet, D.M.; Pielke, R.A.; Pierrehumbert, R.T.; Rhines, P.B.; Stocker, T.F.; Talley, L.D.; et al. Abrupt climate change. *Science* **2003**, *299*, 2005–2010. [CrossRef]
29. Rahmstorf, S. Ocean circulation and climate during the past 120,000 years. *Nature* **2002**, *419*, 207–214. [CrossRef]
30. Duplessy, J.C.; Bard, E.; Arnold, M.; Shackleton, N.J.; Duprat, J.; Labeyrie, L. How fast did the ocean-atmosphere system run during the last deglaciation? *Earth Planet Sci. Lett.* **1991**, *103*, 27–40. [CrossRef]
31. Ou, H.W. Thermohaline circulation: A missing equation and its climate change implications. *Clim. Dyn.* **2018**, *50*, 641–653. [CrossRef]
32. Ou, H.W. A theory of glacier dynamics instabilities Part 1: Topographically confined glaciers. *J. Glaciol.* **2022**, *68*, 1–12. [CrossRef]
33. Calov, R.; Hutter, K. The thermomechanical response of the Greenland ice sheet to various climate scenarios. *Clim. Dyn.* **1996**, *12*, 243–260. [CrossRef]

34. Bond, G.C.; Showers, W.; Elliot, M.; Evans, M.; Lotti, R.; Hajdas, I.; Bonani, G.; Johnson, S. The North Atlantic's 1-2 kyr climate rhythm: Relation to Heinrich events, Dansgaard/Oeschger cycles and the Little Ice Age. In *Mechanisms of Millennial-Scale Global Climate Change*; Clark, P.U., Webb, R., Keigwin, L., Eds.; Geophysical Monograph Series-AGU: Washington, DC, USA, 1999; Volume 112, pp. 35–58.
35. Grousset, F.E.; Labeyrie, L.; Sinko, J.A.; Cremer, M.; Bond, G.; Duprat, J.; Cortijo, E.; Huon, S. Patterns of ice-rafted detritus in the glacial North Atlantic (40–55° N). *Paleoceanography* **1993**, *8*, 175–192. [CrossRef]
36. Raymond, C. Shear margins in glaciers and ice sheets. *J. Glaciol.* **1996**, *42*, 90–102. [CrossRef]
37. Calov, R.; Greve, R.; Abe-Ouchi, A.; Bueler, E.; Huybrechts, P.; Johnson, J.V.; Pattyn, F.; Pollard, D.; Ritz, C.; Saito, F.; et al. Results from the Ice-Sheet Model Intercomparison Project–Heinrich Event INterc0mparison (ISMIP HEINO). *J. Glaciol.* **2010**, *56*, 371–383. [CrossRef]
38. Hemming, S.R. Heinrich events: Massive late Pleistocene detritus layers of the North Atlantic and their global climate imprint. *Rev. Geophys.* **2004**, *42*, 1–43. [CrossRef]
39. Marshall, S.J.; Clarke, G.K. A continuum mixture model of ice stream thermomechanics in the Laurentide Ice Sheet 2. Application to the Hudson Strait Ice Stream. *J. Geophys. Res. Solid Earth* **1997**, *102*, 20615–20637. [CrossRef]
40. Bond, G.; Broecker, W.; Johnsen, S.; McManus, J.; Labeyrie, L.; Jouzel, J.; Bonani, G. Correlations between climate records from North Atlantic sediments and Greenland ice. *Nature* **1993**, *365*, 143–147. [CrossRef]
41. Hooke, R.L. Basal temperatures in polar ice sheets: A qualitative review. *Quat. Res.* **1977**, *7*, 1–13. [CrossRef]
42. Bennett, M.R. Ice streams as the arteries of an ice sheet: Their mechanics, stability and significance. *Earth-Sci. Rev.* **2003**, *61*, 309–339. [CrossRef]
43. Brinkerhoff, D.J.; Johnson, J.V. Dynamics of thermally induced ice streams simulated with a higher-order flow model. *J. Geophys. Res. Earth Surf.* **2015**, *120*, 1743–1770. [CrossRef]
44. Catania, G.A.; Stearns, L.A.; Moon, T.A.; Enderlin, E.M.; Jackson, R.H. Future evolution of Greenland's marine-terminating outlet glaciers. *J. Geophys. Res. Earth Surf.* **2020**, *125*, e2018JF004873. [CrossRef]
45. Stommel, H. Thermohaline convection with two stable regimes of flow. *Tellus* **1961**, *13*, 224–230. [CrossRef]
46. Marotzke, J.; Stone, P. Atmospheric transports, the thermohaline circulation, and flux adjustments in a simple coupled model. *J. Phys. Oceanogr.* **1995**, *25*, 1350–1364. [CrossRef]
47. Manabe, S.; Stouffer, R.J. Two stable equilibria of a coupled ocean-atmosphere model. *J. Clim.* **1988**, *1*, 841–866. [CrossRef]
48. Auer, S.J. Five-year climatological survey of the Gulf Stream system and its associated rings. *J. Geophys. Res.* **1987**, *92*, 11709–11726. [CrossRef]
49. Lozier, M.S. Deconstructing the conveyer belt. *Science* **2010**, *328*, 1507–1511. [CrossRef]
50. Crooks, G.E. Entropy production fluctuation theorem and the nonequilibrium work relation for free energy differences. *Phys. Rev. E* **1999**, *60*, 2721–2726. [CrossRef]
51. Ou, H.W. Possible bounds on the earth's surface temperature: From the perspective of a conceptual global-mean model. *J. Clim.* **2001**, *14*, 2976–2988. [CrossRef]
52. Ozawa, H.; Ohmura, A.; Lorenz, R.D.; Pujol, T. The second law of thermodynamics and the global climate system: A review of the maximum entropy production principle. *Rev. Geophys.* **2003**, *41*. [CrossRef]
53. Kleidon, A. Non-equilibrium thermodynamics and maximum entropy production in the Earth system: Applications and implications. *Naturwiss* **2009**, *96*, 653–677. [CrossRef]
54. Evans, D.J.; Searle, D.J. The fluctuation theorem. *Adv. Phys.* **2002**, *51*, 1529. [CrossRef]
55. Wang, G.M.; Sevick, E.M.; Mittag, E.; Searles, D.J.; Evans, D.J. Experimental demonstration of violations of the Second Law of Thermodynamics for small systems and short time scales. *Phys. Rev. Lett.* **2002**, *89*, 050601. [CrossRef] [PubMed]
56. Peixoto, J.P.; Oort, A.H. *Physics of Climate*; The American Institute of Physics: New York, NY, USA, 1992; p. 520.
57. Kucera, M.; Weinelt, M.; Kiefer, T.; Pflaumann, U.; Hayes, A.; Weinelt, M.; Chen, M.T.; Mix, A.C.; Barrows, T.T.; Cortijo, E.; et al. Reconstruction of sea-surface temperatures from assemblages of planktonic foraminifera: Multi-technique approach based on geographically constrained calibra-tion data sets and its application to glacial Atlantic and Pacific Oceans. *Quat. Sci. Rev.* **2005**, *24*, 951–998. [CrossRef]
58. Macdonald, A.M. The global ocean circulation: A hydrographic estimate and regional analysis. *Progr. Oceanogr.* **1998**, *41*, 281–382. [CrossRef]
59. Sarnthein, M.; Pflaumann, U.; Weinelt, M. Past extent of sea ice in the northern North Atlantic inferred from foraminiferal paleotemperature estimates. *Paleoceanography* **2003**, *18*, 1047. [CrossRef]
60. Heinrich, H. Origin and consequences of cyclic ice rafting in the northeast Atlantic Ocean during the past 130,000 years. *Quat. Res.* **1988**, *29*, 142–152. [CrossRef]
61. Chappell, J. Sea level changes forced ice breakouts in the Last Glacial cycle: New results from coral terraces. *Quat. Sci. Rev.* **2002**, *21*, 1229–1240. [CrossRef]
62. Zahn, R.; Schönfeld, J.; Kudrass, H.R.; Park, M.H.; Erlenkeuser, H.; Grootes, P. Thermohaline instability in the North Atlantic during meltwater events: Stable isotope and ice-rafted detritus records from Core SO75-26KL, Portuguese Margin. *Paleoceanography* **1997**, *12*, 696–710. [CrossRef]
63. Broecker, W.S. Massive iceberg discharges as triggers for global climate change. *Nature* **1994**, *372*, 421–424. [CrossRef]
64. Alley, R.B. Icing the north Atlantic. *Nature* **1998**, *392*, 335–337. [CrossRef]

65. Henry, L.G.; McManus, J.F.; Curry, W.B.; Roberts, N.L.; Piotrowski, A.M.; Keigwin, L.D. North Atlantic ocean circulation and abrupt climate change during the last glaciation. *Science* **2016**, *353*, 470–474. [CrossRef] [PubMed]
66. Broecker, W.S. Paleocean circulation during the last deglaciation: A bipolar seesaw? *Paleoceanography* **1998**, *13*, 119–121. [CrossRef]
67. Stocker, T.F. The seesaw effect. *Science* **1998**, *282*, 61–62. [CrossRef]
68. Clark, P.U.; Alley, R.B.; Pollard, D. Northern Hemisphere ice sheet influences on global climate change. *Science* **1999**, *286*, 1104–1111. [CrossRef]
69. Berger, A. Milankovitch theory and climate. *Rev. Geophys.* **1988**, *26*, 624–657. [CrossRef]
70. Clark, P.U. Surface form of the southern Laurentide Ice Sheet and its implications to ice sheet dynamics. *Geol. Soc. Am. Bull.* **1992**, *104*, 595–605. [CrossRef]
71. Alley, R.B.; Clark, P.U. The deglaciation of the northern hemisphere: A global perspective. *Annu. Rev. Earth Planet Sci.* **1999**, *27*, 149–182. [CrossRef]
72. Bond, G.C.; Lotti, R. Iceberg discharges into the North Atlantic on millennial time scales during the last glaciation. *Science* **1995**, *267*, 1005–1010. [CrossRef]
73. Dansgaard, W.; Johnsen, S.J.; Clausen, H.B.; Dahl-Jensen, D.; Gundestrup, N.S.; Hammer, C.U.; Hvidberg, C.S.; Steffensen, J.P.; Sveinbjörnsdottir, A.E.; Jouzel, J.; et al. Evidence for general instability of past climate from a 250-kyr ice-core record. *Nature* **1993**, *364*, 218–220. [CrossRef]
74. Van Kreveld, S.; Sarnthein, M.; Erlenkeuser, H.; Grootes, P.; Jung, S.; Nadeau, M.J.; Pflaumann, U.; Voelker, A. Potential links between surging ice sheets, circulation changes, and the Dansgaard-Oeschger cycles in the Irminger Sea, 60–18 kyr. *Paleoceanography* **2000**, *15*, 425–442. [CrossRef]
75. Charles, C.D.; Lynch-Stieglitz, J.; Ninnemann, U.S.; Fairbanks, R.G. Climate connections between the hemisphere revealed by deep sea sediment core/ice core correlations. *Earth Planet Sci. Lett.* **1996**, *142*, 19–27. [CrossRef]
76. Lohmann, J.; Ditlevsen, P.D. Objective extraction and analysis of statistical features of Dansgaard–Oeschger events. *Clim. Past* **2019**, *15*, 1771–1792. [CrossRef]
77. Grootes, P.M.; Stuiver, M. Oxygen 18/16 variability in Greenland snow and ice with 103- to 105-year time resolution. *J. Geophys. Res.* **1997**, *102*, 26455–26470. [CrossRef]
78. Oerlemans, J. The mass balance of the Greenland ice sheet: Sensitivity to climate change as revealed by energy-balance modelling. *Holocene* **1991**, *1*, 40–48. [CrossRef]
79. Marshall, S.J.; Koutnik, M.R. Ice sheet action versus reaction: Distinguishing between Heinrich events and Dansgaard-Oeschger cycles in the North Atlantic. *Paleoceanography* **2006**, *21*, 1–13. [CrossRef]
80. Barker, S.; Chen, J.; Gong, X.; Jonkers, L.; Knorr, G.; Thornalley, D. Icebergs not the trigger for North Atlantic cold events. *Nature* **2015**, *520*, 333–336. [CrossRef]
81. Clarke, G.K.; Marshall, S.J.; Veiga-Pires, C.; Bilodeau, G.; Hillaire-Marcel, C. A Glaciological Perspective on Heinrich Events. In *Mechanisms of Global Climate Change at Millennial Time Scales*; Clark, P.U., Webb, R.S., Keigwin, L.D., Eds.; The American Geophysical Union: Washington, DC, USA, 1999; Volume 112, pp. 243–262.
82. Petersen, S.V.; Schrag, D.P.; Clark, P.U. A new mechanism for Dansgaard-Oeschger cycles. *Paleoceanography* **2013**, *28*, 24–30. [CrossRef]
83. Keigwin, L.D.; Jones, G.A.; Lehman, S.J.; Boyle, E.A. Deglacial meltwater discharge, North Atlantic deep circulation, and abrupt climate change. *J. Geophys. Res. Ocean.* **1991**, *96*, 16811–16826. [CrossRef]
84. Fairbanks, R.G. A 17,000-year glacio-eustatic sea level record: Influence of glacial melting rates on the Younger Dryas event and deep-ocean circulation. *Nature* **1989**, *342*, 637–642. [CrossRef]
85. Broecker, W.S.; Andree, M.; Wolfli, W.; Oeschger, H.; Bonani, G.; Kennett, J.; Peteet, D. The chronology of the last deglaciation: Implications to the cause of the Younger Dryas event. *Paleoceanogr. Paleoclimatol.* **1988**, *3*, 1–9. [CrossRef]
86. Teller, J.T. Meltwater and precipitation runoff to the North Atlantic, Arctic, and Gulf of Mexico from the Laurentide ice sheet and adjacent regions during the Younger Dryas. *Paleoceanography* **1990**, *5*, 897–905. [CrossRef]
87. Marchitto, T.M.; Wei, K.Y. History of Laurentide meltwater flow to the Gulf of Mexico during the last deglaciation, as revealed by reworked calcareous nannofossils. *Geology* **1995**, *23*, 779–782. [CrossRef]
88. Lehman, S.J.; Keigwin, J.D. Sudden changes in North Atlantic circulation during the last deglaciation. *Nature* **1992**, *356*, 757–762. [CrossRef]
89. Alley, R.B.; Mayewski, P.A.; Sowers, T.; Stuiver, M.; Taylor, K.C.; Clark, P.U. Holocene climatic instability: A prominent, widespread event 8200 years ago. *Geology* **1997**, *25*, 483–486. [CrossRef]
90. Carlson, A. Why there was not a Younger Dryas-like event during the Penultimate Deglaciation? *Quat. Sci. Rev.* **2008**, *27*, 882–887. [CrossRef]
91. Shakun, J.D.; Clark, P.U.; He, F.; Marcott, S.A.; Mix, A.C.; Liu, Z.; Otto-Bliesner, B.; Schmittner, A.; Bard, E. Global warming preceded by increasing carbon dioxide concentrations during the last deglaciation. *Nature* **2012**, *484*, 49–54. [CrossRef]
92. Clark, P.U.; Pisias, N.G.; Stocker, T.F.; Weaver, A.J. The role of the thermohaline circulation in abrupt climate change. *Nature* **2002**, *415*, 863–869. [CrossRef]
93. McCabe, A.M.; Clark, P.U. Ice-sheet variability around the North Atlantic Ocean during the last deglaciation. *Nature* **1998**, *392*, 373–377. [CrossRef]

94. McManus, J.F.; Oppo, D.W.; Cullen, J.L. A 0.5-million-year record of millennial-scale climate variability in the North Atlantic. *Science* **1999**, *283*, 971–975. [CrossRef]
95. Duplessy, J.C.; Labeyrie, L.; Arnold, M.; Paterne, M.; Duprat, J.; van Weering, T.C. Changes in surface salinity of the North Atlantic Ocean during the last deglaciation. *Nature* **1992**, *358*, 485–488. [CrossRef]
96. Stocker, T.F. Past and future reorganization in the climate system. *Quat. Sci. Rev.* **2000**, *19*, 301–319. [CrossRef]
97. Barker, S.; Diz, P.; Vautravers, M.J.; Pike, J.; Knorr, G.; Hall, I.R.; Broecker, W.S. Interhemispheric Atlantic seesaw response during the last deglaciation. *Nature* **2009**, *457*, 1097–1102. [CrossRef] [PubMed]
98. Denton, G.H.; Anderson, R.F.; Toggweiler, J.R.; Edwards, R.L.; Schaefer, J.M.; Putnam, A.E. The last glacial termination. *Science* **2010**, *328*, 1652–1656. [CrossRef] [PubMed]
99. Alley, R.B.; Meese, D.A.; Shuman, C.A.; Gow, A.J.; Taylor, K.C.; Grootes, P.M.; White, J.W.C.; Ram, M.; Waddington, E.D.; Mayewski, P.A.; et al. Abrupt increase in snow accumulation at the end of the Younger Dryas event. *Nature* **1993**, *362*, 527–529. [CrossRef]